Monthly Notices of the ROYAL ASTRONOMICAL SOCIETY

MNRAS **526,** 1601–1612 (2023) https://doi.org/10.1093/mnras/stad2708
Advance Access publication 2023 September 27

Magnetic fields of low-mass main sequences stars: non-linear dynamo theory and mean-field numerical simulations

N. Kleeorin,[1,2]★ I. Rogachevskii,[1,3]★ N. Safiullin,[2,4] R. Gershberg[5] and S. Porshnev[4,6]

[1]*Department of Mechanical Engineering, Ben-Gurion University of Negev, POB 653, 8410530 Beer-Sheva, Israel*
[2]*Institute of Continuous Media Mechanics, Korolyov str 1, Perm 614013, Russia*
[3]*Nordita, KTH Royal Institute of Technology and Stockholm University, Roslagstullsbacken 23, SE-10691 Stockholm, Sweden*
[4]*Department of Radio Electronic and Informational Technology, Ural Federal University, 19 Mira str, 620002 Ekaterinburg, Russia*
[5]*Crimean Astrophysical Observatory, RAN, 298409 Nauchny, Russia*
[6]*N.N. Krasovskii Institute of Mathematics and Mechanics (IMM UB RAS), 620108 Ekaterinburg, Russia*

Accepted 2023 September 5. Received 2023 September 4; in original form 2023 August 18

ABSTRACT

Our theoretical and numerical analysis have suggested that for low-mass main sequences stars (of the spectral classes from M5 to G0) rotating much faster than the Sun, the generated large-scale magnetic field is caused by the mean-field $\alpha^2\Omega$ dynamo, whereby the α^2 dynamo is modified by a weak differential rotation. Even for a weak differential rotation, the behaviour of the magnetic activity is changed drastically from aperiodic regime to non-linear oscillations and appearance of a chaotic behaviour with increase of the differential rotation. Periods of the magnetic cycles decrease with increase of the differential rotation, and they vary from tens to thousand years. This long-term behaviour of the magnetic cycles may be related to the characteristic time of the evolution of the magnetic helicity density of the small-scale field. The performed analysis is based on the mean-field simulations (MFS) of the $\alpha^2\Omega$ and α^2 dynamos and a developed non-linear theory of α^2 dynamo. The applied MFS model was calibrated using turbulent parameters typical for the solar convective zone.

Key words: dynamo – MHD – turbulence – stars: low-mass – stars: magnetic fields.

1 INTRODUCTION

The cold dwarf stars of the main sequences of the spectral class M composing 70–75 per cent of all star population, have smaller sizes ($0.1\,R_\odot < R < 0.8\,R_\odot$) in comparison with the Sun, smaller masses ($0.08\,M_\odot < M < 0.55\,M_\odot$), smaller luminosity ($L \leq 0.05 L_\odot$) and effective temperatures of 2500–4000 K, where $R_\odot$, $M_\odot$, and $L_\odot$ are the solar radius, mass, and luminosity, respectively (see, e.g. Bochanski et al. 2010; Pecaut & Mamajek 2013; Winters et al. 2019; Kochukhov 2021). About 15–20 per cent of these stars have similar magnetic activity as the Sun with cold magnetic spots and sporadic flares of very high releasing energy in the form of radiations in wide range of wavelength including thermal and non-thermal X-ray (Hawley et al. 2014; Newton et al. 2017). As the Sun, these stars obey differential rotation and have similar atmospheric structure, consisting of photosphere, hot chromosphere, and corona (Wright et al. 2018; Gershberg et al. 2020).

According to various observations (see, e.g. Saar & Linsky 1985; Saar 1996; Donati et al. 2003, 2008; Reiners & Basri 2007), slow rotating stars ($\Omega < \Omega_\odot$) have values and structures of the large-scale magnetic field similar to solar magnetic field, where $\Omega_\odot$ is the solar angular velocity. On the other hand, fast rotating stars ($\Omega > 10\,\Omega_\odot$) have strong poloidal magnetic fields at the pole, and sometimes they have strong toroidal magnetic fields at the pole (Strassmeier 2009; Morin et al. 2010). The periods of the stellar cycles can be in several times larger than the periods of the solar cycles (Bondar', Katsova & Livshits 2019). Magnetic fields of fast rotating stars can be more than several thousands Gauss (Kochukhov et al. 2020; Kochukhov 2021).

Various magnetohydrodynamic (MHD) direct numerical simulations (DNS) and large eddy simulations (LES) of convection and dynamos in low-mass convective stars have been performed in a number of studies (see, e.g. Dobler, Stix & Brandenburg 2006; Browning 2008; Yadav et al. 2016; Brown et al. 2020; Käpylä 2021; Bice & Toomre 2022). They use fully compressible MHD system with weak density stratification or anelastic simulations with strong density stratification in a box or spherical shell. Main results of these simulations are summarized in review by Käpylä et al. (2023). In particular, when the magnetic field is weak or absent, both "solar" and "anti-solar" differential rotation can be formed. When the dynamo generated large-scale magnetic field is strong, it reduces the differential rotation sometimes resulting to the solid-body rotation. The dynamo generated large-scale magnetic field is mainly axisymmetric, and it has the dipole or quadrupole structure depending on rotation, shear, and density stratification. In particular, when rotation is strong and shear is weak, the magnetic field has dipolar structure (Gastine, Duarte & Wicht 2012; Schrinner, Petitdemange & Dormy 2012; Yadav et al. 2015). There are many simulations with highly stratified, vigorous convection that also show dipole magnetic structure (Yadav et al. 2015). In the presence of large-scale shear, propagating dynamo waves are observed in simulations (Yadav et al. 2016; Käpylä 2021; Bice & Toomre 2022). Some simulations also

★ E-mail: nat@bgu.ac.il (NK); gary@bgu.ac.il (IR)

produce non-axisymmetric magnetic field (Käpylä 2021; Bice & Toomre 2022).

Various mean-field dynamo models have been suggested to explain generation of large-scale magnetic fields in M-dwarfs (see, e.g. Chabrier & Küker 2006; Kitchatinov, Moss & Sokoloff 2014; Shulyak et al. 2015; Pipin 2017; Pipin & Yokoi 2018). In particular, mean-field simulations (MFS) of the α^2 dynamo have been performed by Chabrier & Küker (2006). They consider a fully convective rotating star and focus on the kinematic dynamo problem. The large-scale magnetic field is excited when the Coriolis number $\mathrm{Co} = 2\Omega_* \tau \geq 1$, and the dynamo generates a non-axisymmetric steady magnetic field that is symmetric with respect to the equatorial plane (Chabrier & Küker 2006).

Kitchatinov et al. (2014) suggest that M-dwarfs have two types of magnetic activity: (i) magnetic cycles with strong (kilogauss) almost axisymmetric poloidal magnetic fields; and (ii) considerably weaker non-axisymmetric fields with a substantial toroidal component observed at times of magnetic field inversion. To show this, they use a kinematic model of an $\alpha^2\Omega$ dynamo with the differential rotation determined using the numerical mean-field model by Kitchatinov & Olemskoy (2011). Applying this model, they study a magnetic field evolution and find a transition from steady to oscillatory dynamos with increasing turbulent magnetic Prandtl number. Using this approach, Shulyak et al. (2015) suggest four magnetic configurations that appear relevant to dwarfs from the viewpoint of the dynamo theory, and discuss observational tests to identify the configurations observationally.

Pipin (2017) has performed mean-field numerical simulations (MFS) with the non-linear axisymmetric and non-axisymmetric $\alpha^2\Omega$ dynamos of the fully convective star with the mass $M = 0.3\,\mathrm{M}_\odot$ rotating with a period of 10 d. The differential rotation is determined using the numerical mean-field model similar to Kitchatinov & Olemskoy (2011). This dynamo model also includes the meridional circulation, while the magnetic feedback on the non-axisymmetric flows is neglected. The dynamical quenching of the α-effect is described by equation for the total magnetic helicity density. These mean-field numerical simulations yield different dynamo solutions depending on parameters, including variations of the turbulent magnetic Prandtl number, as a key parameter. Increase of this parameter increases the period of the magnetic cycles.

The effects of the cross-helicity in the full-sphere large-scale mean-field dynamo models have been studied by Pipin & Yokoi (2018) in the absence of the differential rotation. They found that non-axisymmetric magnetic field is generated when the cross-helicity and the α-effect operate independently of each other, while their joint action generates preferably axisymmetric dipole magnetic fields.

In this theoretical study and MFS, we show that for the main sequences low-mass fast rotating stars, the generated large-scale magnetic field is due to the mean-field $\alpha^2\Omega$ dynamo, in which the α^2 dynamo is modified by a weak differential rotation. This implies that for this mean-field dynamo $R_\omega \ll R_\alpha R_\alpha^{\rm cr}$, where $R_\omega = (\delta\Omega)\, R_*^2/\eta_{\rm T}$ and $R_\alpha = \alpha_* R_*/\eta_{\rm T}$ are the key dimensionless parameters characterizing the mean-field $\alpha^2\Omega$ dynamo instability, and $R_\alpha^{\rm cr}$ is the threshold required for the excitation of the mean-field dynamo instability, defined by the conditions $\gamma = 0$ and $R_\omega = 0$. Here, R_* is the star radius, $\eta_{\rm T}$ is the turbulent magnetic diffusion coefficient, $\delta\Omega$ is the differential rotation, α_* is the maximum value of the kinetic α-effect, and γ is the dynamo growth rate.

We find that periods of the magnetic activity cycles decrease with increase of the differential rotation, and they can vary from tens to thousand years. The dynamical quenching of the α-effect due to the evolution of the magnetic helicity density of the small-scale field, determines a long-term behaviour of the magnetic cycles.

This paper is organized as follows: In Section 2, we consider the radial profiles of turbulent parameters in a the stellar convective zones, and discuss the theoretical rotating profiles of the kinetic α-effect obtained using theory of the convecting rotating MHD turbulence (Kleeorin & Rogachevskii 2003). In Section 3, we study mean-field $\alpha^2\,\Omega$ dynamo, where we start with the kinematic $\alpha^2\,\Omega$ dynamo (Section 3.1), discuss the algebraic and dynamic non-linearities (Section 3.2), and continue with MFS of the $\alpha^2\Omega$ dynamo (Section 3.3) as well as the α^2 dynamo (Section 3.4). In Section 4, we develop non-linear theory of axisymmetric α^2 dynamo. Finally, in Section 5, we discuss the obtained results, compare various numerical models and outline conclusions.

2 RADIAL PROFILES OF TURBULENT PARAMETERS IN THE STELLAR CONVECTIVE ZONES

In this Section, we discuss radial profiles of various turbulent parameters in the stellar convective zones. As a turbulent model of stellar convective zones, we use "Modules for Experiments in Stellar Astrophysics (MESA)" (Paxton et al. 2011). The MESA (http://mesa.sourceforge.net/) is one-dimensional stellar evolution module, which combines many of the numerical and physics modules for simulations of a wide range of stellar evolution scenarios ranging from very low mass to massive stars.

The MESA includes a module which implements the standard mixing length theory (MLT) of convection (Cox & Giuli 1968), as well as the modified MLT (Henyey, Vardya & Bodenheimer 1965). Whereas the standard MLT assumes high-optical depths and no radiative losses, the modified MLT allows the convective efficiency to vary with the opaqueness of the convective element, which is an important effect for convective zones near the outer layers of stars (Henyey et al. 1965).

Using the MESA, we plot the radial profiles of the convective turbulent velocity $u_{\rm c}$ (Fig. 1), the turbulent magnetic diffusivity η_T (Fig. 2) and the Coriolis parameter $\Omega_\odot \tau(r)$ (Fig. 3) based on the solar angular velocity $\Omega_\odot$ and the turbulent turn-over time $\tau(r) = 3\eta_{\rm T}/u_{\rm c}^2$ for stars of late spectral classes: M6, M4, M2, K7, K4, K2, and G2. Here, H_* is the thickness of the convective zone, h is the height from the bottom of the convective zone, the velocity is measured in $\mathrm{cm\,s^{-1}}$, and R_* is the star radius. Depending on the spectral class and the depth of the convective zone, the convective turbulent velocity $u_{\rm c}$ changes from 10^2 to $10^5\ \mathrm{cm\,s^{-1}}$. Strong changes in $u_{\rm c}$ occur in the upper part of the convective zone (see Fig. 1).

On the other hand, the turbulent magnetic diffusivity $\eta_{\rm T}$ varies inside the convective zone only in several times for stars of the spectral classes from M2 to G2, while it changes by two orders of magnitude for stars of the spectral classes from M4 and M6 (see Fig. 2). The Coriolis parameter $\Omega_\odot \tau(r)$ based on the solar angular velocity $\Omega_\odot$ and the turbulent turn-over time $\tau(r) = 3\eta_{\rm T}/u_{\rm c}^2$ strongly decreases from 10^2 near the base of the convective zone to 10^{-2}–10^{-4} near the star surface depending on the spectral class (see Fig. 3). Note that models of the solar convective zone are given by Baker & Temesvary (1966) and Spruit (1974).

Models of the stellar convective zones based on the standard mixing length theory do not take into account the effect of the Coriolis force on the convective turbulence. One of the key effects of rotation in density-stratified convection is

(i) production of the kinetic helicity and the kinetic α-effect,

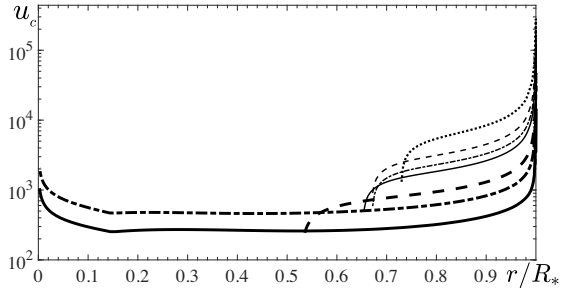

Figure 1. The radial profiles of the convective turbulent velocity u_c for the main sequences stars of the spectral classes: M6 (thick solid); M4 (thick dashed–dotted); M2 (thick dashed); K7 (thin solid); K4 (thin dashed-dotted); K2 (thin dashed); G2 (thin dotted). The velocity is measured in cm s^{-1}. Here, R_* is the star radius.

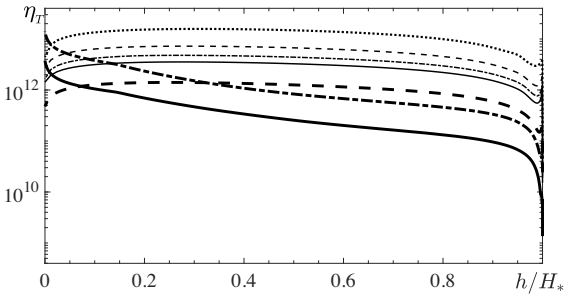

Figure 2. The radial profiles of the turbulent magnetic diffusivity η_T for the main sequences stars of the spectral classes: M6 (thick solid); M4 (thick dashed–dotted); M2 (thick dashed); K7 (thin solid); K4 (thin dashed–dotted); K2 (thin dashed); G2 (thin dotted). The turbulent magnetic diffusivity is measured in cm^2 s^{-1}. Here, H_* is the thickness of the convective zone, and h is the height from the bottom of the convective zone.

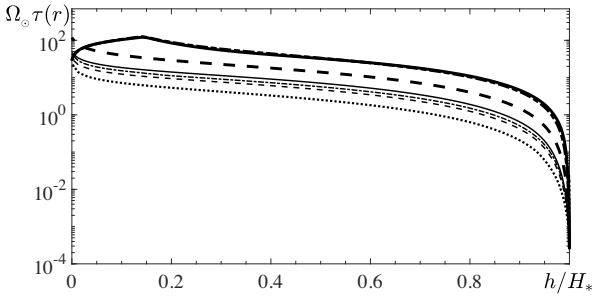

Figure 3. The radial profiles of the Coriolis parameter $\Omega_\odot \tau(h)$ based on the solar angular velocity $\Omega_\odot$ and the turbulent turn-over time $\tau(r) = 3\eta_T/u_c^2$ for the main sequences stars of the spectral classes: M6 (thick solid); M4 (thick dashed–dotted); M2 (thick dashed); K7 (thin solid); K4 (thin dashed–dotted); K2 (thin dashed); G2 (thin dotted). The turbulent magnetic diffusivity is measured in cm^2 s^{-1}.

(ii) formation of the differential rotation and
(iii) strong anisotropization of turbulence.

Using the results obtained applying the theory of the convecting rotating MHD turbulence (Kleeorin & Rogachevskii 2003; Brandenburg et al. 2013), we plot in Figs 4–7 the isotropic part of the kinetic $\boldsymbol{\alpha}$ tensor that characterizes the kinetic $\boldsymbol{\alpha}$-effect,

$$\alpha = \frac{1}{6}\left(\frac{\ell_0^2\Omega}{H_\rho}\right)\sin\phi\,\left[\Psi_1(\omega) + \Psi_2(\omega)\sin^2\phi\right], \qquad (1)$$

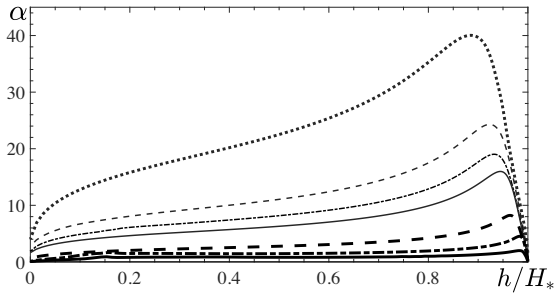

Figure 4. The radial profiles of the kinetic α-effect at the pole (at the latitude $\phi = \pi/2$) for isotropic turbulent convection for $\sigma = 1$ and $\varepsilon = 0$ for the main sequences stars of the spectral classes: M6 (thick solid); M4 (thick dashed–dotted); M2 (thick dashed); K7 (thin solid); K4 (thin dashed–dotted); K2 (thin dashed); G2 (thick dotted). The kinetic α is measured in m s^{-1}.

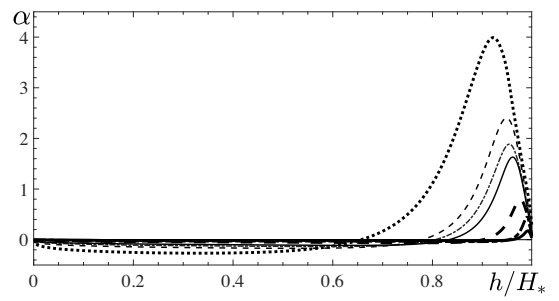

Figure 5. The radial profiles of the kinetic α-effect at the latitude $\phi = \pi/6$ for anisotropic turbulent convection for $\sigma = 2$ and $\varepsilon = 1.2$ for the main sequences stars of the spectral classes: M6 (thick solid); M4 (thick dashed–dotted); M2 (thick dashed); K7 (thin solid); K4 (thin dashed–dotted); K2 (thin dashed); G2 (thick dotted). The kinetic α is measured in m s^{-1}.

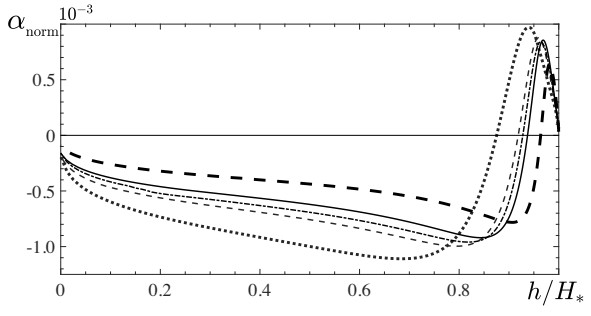

Figure 6. The radial profiles of the normalized kinetic α-effect, $\alpha_{\rm norm} = \alpha/(\Omega_\odot\,\eta_{\rm T})^{1/2}$, at the pole ($\phi = \pi/2$) for $\sigma = 2$ and $\varepsilon = 1.2$, for the main sequences stars with the solar rotation rate of the spectral classes: M6 (thick solid); M4 (thick dashed–dotted); M2 (thick dashed); K7 (thin solid); K4 (thin dashed–dotted); K2 (thin dashed); G2 (thick dotted). Here, H_* is the height of the convective zone, and h is the height from the bottom of the convective zone.

where ϕ is the latitude, Ω is the angular velocity, H_ρ is the density stratification height, ℓ_0 is the integral scale of turbulent convection, the parameter $\omega = 4\Omega\tau(r)$, and the functions $\Psi_1(\omega)$ and $\Psi_2(\omega)$ are given in Appendix A.

For instance, for a slow rotation ($\omega \ll 1$), the kinetic α-effect is given by

$$\alpha = \frac{4}{5}\left(\frac{\ell_0^2\Omega}{H_\rho}\right)\left(2 - \frac{\sigma}{3} - \frac{5\lambda}{6}\right)\sin\phi\,, \qquad (2)$$

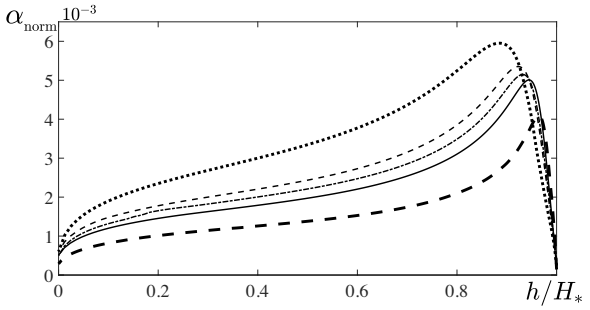

Figure 7. The radial profiles of the normalized kinetic α-effect, $\alpha_{\rm norm} = \alpha/(10\Omega_\odot\,\eta_{\rm T})^{1/2}$, at the pole ($\phi = \pi/2$) for $\sigma = 1$ and $\varepsilon = 0$, for the main sequences stars of the spectral classes: M6 (thick solid); M4 (thick dashed–dotted); M2 (thick dashed); K7 (thin solid); K4 (thin dashed–dotted); K2 (thin dashed); G2 (thick dotted). Here, H_* is the height of the convective zone, and h is the height from the bottom of the convective zone.

Table 1. The coefficient C_* for different spectral classes and different rotation rates.

Spectral class	$\Omega_\odot$	$10\Omega_\odot$	$20\Omega_\odot$
G2	0.970	0.933	0.982
K2	0.877	0.874	0.883
K4	0.824	0.858	0.854
K7	0.855	0.815	0.793
M2	0.643	0.687	0.680

and for fast rotation ($\omega \gg 1$) it is given by

$$\alpha = -\frac{\pi}{32}\left(\frac{\ell_0 u_c}{H_\rho}\right)\left(2\lambda + \frac{\sigma}{3} - 3 + (\sigma - 1)\sin^2\phi\right)\sin\phi, \tag{3}$$

where $u_{\rm c} = \ell_0/\tau$ is the characteristic turbulent velocity. Here, the parameter $\lambda = 2\varepsilon/(\varepsilon + 2)$ is related to the degree of anisotropy ε of turbulent velocity field:

$$\varepsilon = \frac{2}{3}\left(\frac{\langle \mathbf{u}_\perp^2\rangle}{\langle \mathbf{u}_z^2\rangle} - 2\right), \tag{4}$$

$\mathbf{u}_\perp$ is the horizontal turbulent velocity, $\mathbf{u}_z$ is the vertical turbulent velocity (in the direction of gravity). The parameter σ determines the degree of thermal anisotropy. For $\sigma < 1$, the thermal plumes in a convective turbulence have the form of column or thermal jets, while for $\sigma > 1$, the ''pancake" thermal plumes exist in the background turbulent convection.

For example, in Fig. 4, we show the radial profiles of the kinetic α-effect at the pole (at the latitude $\phi = \pi/2$) for isotropic turbulent convection for $\sigma = 1$ and $\varepsilon = 0$, while in Fig. 5, we plot the kinetic α-effect at the latitude $\phi = \pi/6$ for anisotropic turbulent convection for $\sigma = 2$ and $\varepsilon = 1.2$. Various curves in Figs 4 and 5 correspond to stars of the spectral classes from M6 to G2. We use here the radial profile of the Coriolis parameter $\Omega_\odot\tau(r)$ to determine the radial profile of the kinetic $\boldsymbol{\alpha}$-effect which is the function of the Coriolis parameter. It follows from Figs 4 and 5 that the maximum value α_* of the kinetic α-effect depends on the spectral class at a given rotation rate. For instance, the stars of the spectral class G2 have largest values of α_*, while the stars of the spectral class M6 have smallest α_*. The anisotropy of the convective turbulence decreases the values of α_* and causes a localization of the maximum value of the kinetic α-effect at the vicinity of the star surface and the equator.

The maximum value of the kinetic α-effect can be estimated as (Kleeorin, Rogachevskii & Ruzmaikin 1995):

$$\alpha_* = C_*(\Omega_*\,\eta_{\rm T})^{1/2}, \tag{5}$$

where the coefficient C_* is given in Table 1 for different spectral classes and different rotation rates. It follows from Table 1 that the coefficient C_* is weakly dependent on the rotation rates. To derive equation (5), we use a spatial distribution of the kinetic α-effect. In particular, the kinetic α-effect is $\alpha \simeq \ell(r)\Omega_*$ for $\ell(r)\Omega_*/u_{\rm c}(r) \ll 1$, and $\alpha \simeq u_{\rm c}(r)$ for $\ell(r)\Omega_*/u_{\rm c}(r) \gg 1$ (Zeldovich, Ruzmaikin & Sokoloff 1983). The kinetic α-effect reaches a maximum at the depth $r = r_{\rm m}$ determined by the condition $\ell_{\rm m}(r_{\rm m}) = u_{\rm c}(r_{\rm m})/\Omega_*$. The turbulent magnetic diffusivity is $\eta_{\rm T} \simeq \ell_{\rm m}(r_{\rm m})u_{\rm c}(r_{\rm m})$. Therefore, $\ell_{\rm m}(r_{\rm m}) \simeq (\eta_{\rm T}/\Omega_*)^{1/2}$. The maximal value of the kinetic α-effect, α_*, is given by $\alpha_* \simeq u_{\rm c}(r_{\rm m}) \simeq \eta_{\rm T}/\ell_{\rm m}(r_{\rm m}) \simeq (\eta_{\rm T}\Omega_*)^{1/2}$.

In Figs 6 and 7, we show the radial profiles $\alpha_{\rm norm} = \alpha/(\Omega_\odot\,\eta_{\rm T})^{1/2}$ of the kinetic α-effect normalized by $(\Omega_\odot\,\eta_{\rm T})^{1/2}$. This normalization and anisotropy of the convective turbulence cause the curves of the different spectral classes $\alpha_{\rm norm}$ almost collapse to each other. This indicates that the estimate (5) is enough good. In this study, we will use this estimate to determine the dynamo number (see below).

3 MEAN-FIELD $\alpha^2\,\Omega$ DYNAMO

Mean-field theories of solar, stellar, and galactic dynamos have been developing during last 55 yr (see, e.g. books by Moffatt 1978; Parker 1979; Krause & Rädler 1980; Zeldovich et al. 1983; Ruzmaikin, Shukurov & Sokoloff 1988; Rüdiger, Hollerbach & Kitchatinov 2013; Moffatt & Dormy 2019; Rogachevskii 2021; Shukurov & Subramanian 2021). In this study, we show that magnetic field generation in fast rotating stars of the spectral classes: from M6 to G0 can be described by the axisymmetric mean-field $\alpha^2\,\Omega$ dynamo, where the α^2 dynamo is modified by a weak differential rotation with $R_\omega \ll R_\alpha R_\alpha^{\rm cr}$. The axisymmetric large-scale magnetic field can be written as $\overline{\boldsymbol{B}} = \overline{B}_\varphi \boldsymbol{e}_\varphi + \boldsymbol{\nabla}\times(\overline{A}\boldsymbol{e}_\varphi)$, where r, θ, φ are the spherical coordinates and $\boldsymbol{e}_\varphi$ is the unit vector. We consider the mean-field dynamo in a thin convective shell, taking into account strong variation of the plasma density in the radial direction (see below). We neglect the curvature of the convective shell and replace it by a flat slab. Thus, the mean-field $\alpha^2\,\Omega$ dynamo equations are given by:

$$\frac{\partial \overline{B}_\varphi}{\partial t} = \left[R_\alpha\,R_\omega\,\sin\theta\,\frac{\partial}{\partial\theta} - R_\alpha^2\left(\frac{\partial^2}{\partial\theta^2} - \mu^2\right)\right]\overline{A} + \left(\frac{\partial^2}{\partial\theta^2} - \mu^2\right)\overline{B}_\varphi, \tag{6}$$

$$\frac{\partial \overline{A}}{\partial t} = \alpha\overline{B}_\varphi + \left(\frac{\partial^2}{\partial\theta^2} - \mu^2\right)\overline{A}. \tag{7}$$

To take into account strong variation of the plasma density in the radial direction, we average the dynamo equations over the depth of the convective zone and use the no-r model. In particular, the terms describing turbulent diffusion of the mean magnetic field in the radial direction in equations (6) and (7) in the framework of the no-r model are given as $-\mu^2\overline{B}_\varphi$ and $-\mu^2\overline{A}$ (Kleeorin et al. 2003a, 2016; Safiullin et al. 2018). The differential rotation is characterized by parameter $G = \partial\Omega/\partial r$, and the parameter μ is determined by the following equation: $\int_{r_{\rm c}}^1(\partial^2\overline{B}_\varphi/\partial r^2)\,{\rm d}r = -(\mu^2/3)\overline{B}_\varphi$.

Equations (6) and (7) are written in dimensionless variables: the coordinate r is measured in the units of the star radius R_*, the time t is measured in the units of turbulent magnetic diffusion time $R_*^2/\eta_{\rm T}$; the toroidal component, $\overline{B}_\varphi(t, r, \theta)$, of the mean magnetic field is measured in the units of B_*, where $B_* \equiv \xi\ \overline{B}_{\rm eq}$, $\xi = \ell_0/\sqrt{2}R_*$ and

$\overline{B}_{\rm eq} = u_0\sqrt{4\pi\overline{\rho}_*}$. The magnetic potential, $\overline{A}(t, r, \theta)$, of the poloidal field is measured in the units of $R_\alpha R_* B_*$, where $R_\alpha = \alpha_* R_*/\eta_{\rm T}$, the fluid density $\overline{\rho}(r, \theta)$ is measured in the units $\overline{\rho}_*$, the differential rotation $\delta\Omega$ is measured in units of the maximal value of the angular velocity Ω, the α-effect is measured in units of the maximum value of the kinetic α-effect, α_*; the integral scale of the turbulent motions ℓ_0, and the characteristic turbulent velocity u_0 at the scale ℓ_0 are measured in units of their maximum values in the convective region. The magnetic Reynolds number ${\rm Rm} = \ell_0 u_0/\eta$ is defined using the maximal values of the integral scale ℓ_0 and the characteristic turbulent velocity u_0, and the turbulent magnetic diffusion coefficient is $\eta_{\rm T} = \ell_0 u_0/3$. The dynamo number is defined as $D = R_\alpha R_\omega$, where $R_\omega = (\delta\Omega)\, R_*^2/\eta_{\rm T}$.

Equations (6) and (7) describe the dynamo waves propagating from the central latitudes towards the equator when the dynamo number is negative. The radius r varies from $r_{\rm c}$ to 1 inside the convective shell, so that, e.g. for stars of the spectral class G2 (the solar-like stars), the value $\mu = 3$ corresponds to a convective zone with a thickness of about 1/3 of the radius.

3.1 Kinematic $\alpha^2\,\Omega$ dynamo

First, we consider a kinematic dynamo problem, assuming for simplicity that the kinetic α-effect is a constant. Note that the kinematic and weakly nonlinear $\alpha^2\Omega$ dynamos have been studied in a number of publications (see, e.g., Meunier et al. 1996; Griffiths et al. 2001; Bassom et al. 2005, and references therein). We seek a solution for equations (6) and (7) as a real part of the following functions:

$$\overline{A} = A_0 \exp(\tilde{\gamma} t - {\rm i}\, k\, \theta), \tag{8}$$

$$\overline{B}_\varphi = B_0 \exp(\tilde{\gamma} t - {\rm i}\, k\, \theta), \tag{9}$$

where $\tilde{\gamma} = \gamma + {\rm i}\,\omega$. Equations (6)–(9) yield the growth rate of the dynamo instability and the frequency of the dynamo waves as

$$\gamma = \frac{R_\alpha R_\alpha^{\rm cr}}{\sqrt{2}} \left[\left[1 + \left(\frac{\zeta R_\omega}{R_\alpha R_\alpha^{\rm cr}} \right)^2 \right]^{1/2} + 1 \right]^{1/2} - \left(R_\alpha^{\rm cr} \right)^2, \tag{10}$$

$$\omega = -{\rm sgn}(R_\omega)\, \frac{R_\alpha R_\alpha^{\rm cr}}{\sqrt{2}} \left[\left[1 + \left(\frac{\zeta R_\omega}{R_\alpha R_\alpha^{\rm cr}} \right)^2 \right]^{1/2} - 1 \right]^{1/2}, \tag{11}$$

where $\zeta^2 = 1 - \left(\mu/R_\alpha^{\rm cr}\right)^2$. Here we took into account that $(x + {\rm i}y)^{1/2} = \pm(X + {\rm i}Y)$, where $X = 2^{-1/2}\,[(x^2 + y^2)^{1/2} + x]^{1/2}$ and $Y = {\rm sgn}(y)\, 2^{-1/2}\,[(x^2 + y^2)^{1/2} - x]^{1/2}$. Here the threshold $R_\alpha^{\rm cr}$ for the mean-field dynamo instability, defined by the conditions $\gamma = 0$ and $R_\omega = 0$, is given by $R_\alpha^{\rm cr} = (k^2 + \mu^2)^{1/2}$.

Equations (6)–(9) allow one to determine the squared amplitude ratio $|A_0/B_0|^2$ as:

$$\left| \frac{A_0}{B_0} \right|^2 = \left(R_\alpha R_\alpha^{\rm cr} \right)^{-2} \left[1 + \left(\frac{\zeta R_\omega}{R_\alpha R_\alpha^{\rm cr}} \right)^2 \right]^{-1/2}, \tag{12}$$

and the phase shift δ between the toroidal field $\overline{B}_\varphi$ and the vector potential $\overline{A}$ is given by the following equation:

$$\sin(2\delta) = -\zeta R_\omega \left[\left(R_\alpha R_\alpha^{\rm cr} \right)^2 + \zeta^2 R_\omega^2 \right]^{-1/2}. \tag{13}$$

Equation (12) yields the energy ratio of poloidal $\overline{B}_{\rm pol} = R_\alpha R_\alpha^{\rm cr}\, \overline{A}$ and toroidal $\overline{B}_\varphi$ mean magnetic field components as:

$$\frac{\overline{B}_{\rm pol}^2}{\overline{B}_\varphi^2} = \left[1 + \left(\frac{\zeta R_\omega}{R_\alpha R_\alpha^{\rm cr}} \right)^2 \right]^{-1/2}. \tag{14}$$

Asymptotic formulas for the growth rate of the dynamo instability and the frequency of the dynamo waves for a weak differential rotation, $\zeta R_\omega \ll R_\alpha R_\alpha^{\rm cr}$, are given by

$$\gamma = R_\alpha R_\alpha^{\rm cr} \left[1 + \frac{1}{8} \left(\frac{\zeta R_\omega}{R_\alpha R_\alpha^{\rm cr}} \right)^2 \right] - \left(R_\alpha^{\rm cr} \right)^2, \tag{15}$$

$$\omega = -\frac{\zeta R_\omega}{\sqrt{2}}. \tag{16}$$

In this case, the mean-field α^2 dynamo is slightly modified by a weak differential rotation, and the phase shift between the fields $\overline{B}_\varphi$ and $\overline{B}_\theta$ vanishes, while $\overline{B}_{\rm pol}/\overline{B}_\varphi \sim 1$ (see equations 13 and 14). The period of the dynamo wave is $T_{\rm dyn} = (2\pi/\omega)\,(R_*^2/\eta_{\rm T})$, where ω is the non-dimensional frequency of the dynamo wave given by equation (16). In this study, we show that this case corresponds to fast rotating stars of the spectral class from M6 to G0. Since in this case $\overline{B}_{\rm pol} \sim \overline{B}_\varphi$, the star spots can be formed for any latitude.

In the opposite case, for a strong differential rotation, $\zeta R_\omega \gg R_\alpha R_\alpha^{\rm cr}$, the growth rate of the dynamo instability and the frequency of the dynamo waves are given by

$$\gamma = \left[\frac{1}{2}\, \zeta\, R_\alpha^{\rm cr}\, R_\alpha |R_\omega| \right]^{1/2} - \left(R_\alpha^{\rm cr} \right)^2, \tag{17}$$

$$\omega = -{\rm sgn}(R_\omega) \left[\frac{1}{2}\, \zeta\, R_\alpha^{\rm cr}\, R_\alpha |R_\omega| \right]^{1/2}. \tag{18}$$

In this case the mean-field $\alpha\Omega$ dynamo is slightly modified by a weak α^2 effect, and the phase shift between the fields $\overline{B}_\varphi$ and $\overline{B}_\theta$ tends to $-\pi/4$, while $\overline{B}_{\rm pol}/\overline{B}_\varphi \ll 1$ (see equations 13 and 14). This case corresponds to the solar dynamo. The necessary condition for the dynamo ($\gamma > 0$) is:

(a) when $R_\alpha/R_\alpha^{\rm cr} < \sqrt{2}$, the mean-field $\alpha^2\,\Omega$ dynamo is excited when

$$D > \frac{2}{\zeta} \left(R_\alpha^{\rm cr} \right)^3; \tag{19}$$

(b) when $R_\alpha/R_\alpha^{\rm cr} > \sqrt{2}$, the mean-field $\alpha^2\,\Omega$ dynamo is excited for any differential rotation, R_ω.

3.2 Algebraic and dynamic non-linearities

Now, we discuss the algebraic and dynamic non-linearities in the non-linear dynamo model. The total α-effect is the sum of the kinetic and magnetic α-effects,

$$\alpha = \chi_{\rm K}\, \Phi_{\rm K}(\overline{B}) + \sigma_\rho\, \chi_{\rm M}\, \Phi_{\rm M}(\overline{B}), \tag{20}$$

where $\chi_{\rm K} = -(\tau_0/3)\, \langle \boldsymbol{u} \cdot (\nabla \times \boldsymbol{u}) \rangle$ is proportional to the kinetic helicity $\langle \boldsymbol{u} \cdot (\nabla \times \boldsymbol{u}) \rangle$ and $\chi_{\rm M} = (\tau_0/12\pi\,\overline{\rho})\, \langle \boldsymbol{b} \cdot (\nabla \times \boldsymbol{b}) \rangle$ is proportional to the current helicity $\langle \boldsymbol{b} \cdot (\nabla \times \boldsymbol{b}) \rangle$ (Frisch et al. 1975; Pouquet, Frisch & Leorat 1976). Here, τ_0 is the correlation time of the turbulent velocity field, $\boldsymbol{u}$ and $\boldsymbol{b}$ are velocity and magnetic fluctuations, and $\sigma_\rho = \int_{r_{\rm c}}^1 (\overline{\rho}(r)/\overline{\rho}_*)^{-1}\, {\rm d}r$ (Kleeorin et al. 2016; Safiullin et al. 2018).

The quenching functions $\Phi_{\rm K}(\overline{B})$ and $\Phi_{\rm M}(\overline{B})$ in equation for the total α-effect are given by (Rogachevskii & Kleeorin 2000, 2001, 2004, 2006),

$$\Phi_{\rm K}(\overline{B}) = \frac{1}{7} \left[4\Phi_{\rm M}(\overline{B}) + 3\Phi_{\rm B}(\overline{B}) \right], \tag{21}$$

and (Field, Blackman & Chou 1999)

$$\Phi_{\rm M}(\overline{B}) = \frac{3}{8\beta^2}\left[1 - \frac{\arctan(\sqrt{8}\beta)}{\sqrt{8}\beta}\right], \quad (22)$$

where $\beta = \overline{B}/\overline{B}_{\rm eq}$

$$\Phi_{\rm B}(\overline{B}) = 1 - 16\beta^2 + 128\beta^4 \ln\left[1 + (8\beta^2)^{-1}\right], \quad (23)$$

and $\chi_{\rm K}$ and $\chi_{\rm M}$ are measured in units of maximal value of the α-effect, α_*. The function $\Phi_{\rm K}$ describes the algebraic quenching of the kinetic α-effect that is caused by the feedback effects of the mean magnetic field on plasma motions. The densities of the kinetic and current helicities, and quenching functions are associated with a middle part of the convective zone. The parameter $\sigma_\rho > 1$ is a free parameter.

The magnetic α-effect, $\alpha_{\rm M}$, is based on two non-linearities: the algebraic non-linearity due to the feedback effects of the mean magnetic field on plasma motions, that is described by the quenching function $\Phi_{\rm M}(\overline{B})$, and the dynamic non-linearity, characterized by the function $\chi_{\rm M}(\overline{\boldsymbol{B}})$ that is determined by a dynamical equation (Kleeorin & Ruzmaikin 1982; Gruzinov & Diamond 1994; Kleeorin & Rogachevskii 1999; Kleeorin et al. 1995; 2000, 2002, 2003a, b; Blackman & Field 2000; Brandenburg & Subramanian 2005; Zhang et al. 2006, 2012). In particular, the total magnetic helicity, $\int (H_{\rm M} + H_{\rm m})\, {\rm d}r^3$, is conserved for very small microscopic magnetic diffusivity η, where $H_{\rm M} = \overline{\boldsymbol{A}}\cdot\overline{\boldsymbol{B}}$ is the magnetic helicity density of the large-scale field $\overline{\boldsymbol{B}} = \nabla\times\overline{\boldsymbol{A}}$ with $\overline{\boldsymbol{A}}$ being the mean magnetic vector potential, $H_{\rm m} = \langle \boldsymbol{a}\cdot\boldsymbol{b}\rangle$ is the magnetic helicity density of the small-scale field $\boldsymbol{b} = \nabla\times\boldsymbol{a}$ with $\boldsymbol{a}$ being fluctuations of magnetic vector potential.

When the mean-field dynamo amplifies the large-scale magnetic field, the magnetic helicity density $H_{\rm M}$ of the large-scale field grows in time. Since the total magnetic helicity $\int (H_{\rm M} + H_{\rm m})\, {\rm d}r^3$ is conserved, the magnetic helicity density $H_{\rm m}$ of the small-scale field changes during the dynamo action, and its evolution is determined by the non-dimensional dynamical equation (Kleeorin et al. 2016; Safiullin et al. 2018):

$$\frac{\partial \chi_{\rm c}}{\partial t} + \left(\tau_\chi^{-1} + \kappa_{\rm T}\mu^2\right)\chi_{\rm c} = 2\left(\frac{\partial \overline{\rm A}}{\partial\theta}\frac{\partial \overline{B}_\varphi}{\partial\theta} + \mu^2 \overline{\rm A}\,\overline{B}_\varphi\right)$$
$$-\alpha\,\overline{B}^2 - \frac{\partial}{\partial\theta}\left(\overline{B}_\varphi\frac{\partial \overline{\rm A}}{\partial\theta} - \kappa_{\rm T}\frac{\partial \chi^c}{\partial\theta}\right), \quad (24)$$

where $\boldsymbol{F}_\chi = -\kappa_{\rm T}\nabla\chi_{\rm c}$ is the turbulent diffusion flux of the magnetic helicity density of small-scale field and $\kappa_{\rm T}$ is the coefficient of the turbulent diffusion of the magnetic helicity. Dynamics of magnetic helicity of small-scale field is a crucial mechanism in a non-linear dynamo saturation where turbulent magnetic helicity fluxes allow to avoid catastrophic quenching of the α-effect. Recently, turbulent fluxes of magnetic helicity density of small-scale magnetic field have been rigorously derived by Kleeorin & Rogachevskii (2022) and Gopalakrishnan & Subramanian (2023).

In equation (24), the time $\tau_\chi = \ell^2/\eta$ is the relaxation time of magnetic helicity. The average value of τ_χ^{-1} is given by

$$\tau_\chi^{-1} = H_*^{-1}\int_{r_{\rm c}}^{1}\tilde{\tau}_\chi^{-1}(r)\,{\rm d}r \sim \frac{H_\ell\, R_*^2\,\eta}{H_*\,\ell^2\,\eta_{\rm T}}, \quad (25)$$

where H_* is the depth of the convective zone, H_ℓ is the characteristic scale of variations ℓ_0, and $\tilde{\tau}_\chi(r) = (\eta_{\rm T}/R_*^2)(\ell_0^2/\eta)$ is the non-dimensional relaxation time of the density of the magnetic helicity. The values H_ℓ, η, ℓ_0 in equation (25) are associated with the upper part of the convective zone. The mean magnetic field is given by

$$\overline{B}^2 = \overline{B}_\varphi^2 + R_\alpha^2\left[\mu^2\overline{\rm A}^2 + \left(\frac{\partial \overline{\rm A}}{\partial\theta}\right)^2\right]. \quad (26)$$

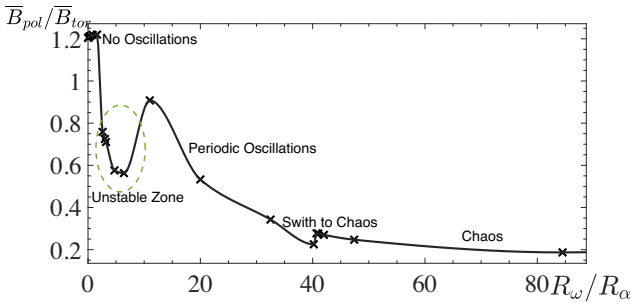

Figure 8. The ratio of the maximum values of the poloidal to toroidal mean magnetic fields $\overline{B}_{\rm pol}/\overline{B}_{\rm tor}$ versus R_ω/R_α obtained from numerical simulations of $\alpha^2\Omega$ mean-field dynamo.

3.3 Mean-field numerical simulations of the $\alpha^2\Omega$ dynamo

We perform MFS of the $\alpha^2\Omega$ dynamo by solving numerically equations (6), (7), and (24). We use MATLAB code, which solves initial-boundary value problems for systems of parabolic and elliptic partial-differential equations that employs a second-order explicit finite differences in space. We use the spatial resolution of 203 mesh points in co-latitude θ (this odd number provides mesh intervals below 1 degree). The time grid in simulations varied between 6×10^5 and 18×10^5 time instants for a different set of initial parameters due to long transitional processes.

For numerical simulations, we use the standard profile of the kinetic α-effect: $\alpha(\theta) = \alpha_0\sin^3\theta\cos\theta$. We use the following initial conditions: $\overline{B}_\phi(t=0,\theta) = S_1\sin\theta + S_2\sin(2\theta)$ and $\overline{\rm A}(t=0,\theta) = 0$ corresponding to a combination of the dipole and quadropole type solutions. The parameters of the numerical simulation are as follows: $G = 1$, $\xi = 0.1$, $\kappa_{\rm T} = 0.1$, $T = 6.3$, $S_1 = 0.051$, $S_2 = 0.95$ for different μ, R_α, and R_ω. These parameters and initial conditions have been used by us for modelling of the solar activity by the axisymmetric mean-field $\alpha\,\Omega$ dynamo (Kleeorin et al. 2016, 2020; Safiullin et al. 2018), where mechanism of the sunspot formation related to negative effective magnetic pressure instability have been taken into account (Kleeorin, Rogachevskii & Ruzmaikin 1989, 1990; Kleeorin & Rogachevskii 1994; Kleeorin, Mond & Rogachevskii 1996; Rogachevskii & Kleeorin 2007; Brandenburg et al. 2011; Warnecke et al. 2013, 2016; Brandenburg, Rogachevskii & Kleeorin 2016).

First we perform numerical simulations of the $\alpha^2\Omega$ mean-field dynamo at $R_\alpha = 10$. This value of the parameter R_α corresponds to the kinetic α-effect arising in rotating convective turbulence with the rotating frequency that is in 25 times larger than that for the Sun. In Fig. 8, we plot the ratio of the maximum values of the poloidal to toroidal mean magnetic fields $\overline{B}_{\rm pol}/\overline{B}_{\rm tor}$ versus R_ω/R_α. Depending on the ratio R_ω/R_α, there are ranges of the aperiodic behaviouur, the quasi-periodic oscillations of the mean magnetic field, and the chaotic behaviour. This is seen in Fig. 9, where we show the time evolution of the flux of the toroidal mean magnetic field $\Phi = \int|\overline{B}_\varphi|\,{\rm d}\sigma$ obtained from numerical simulations of the $\alpha^2\Omega$ mean-field dynamo for different values of R_ω/R_α =1.6, 3.2, 4.7, and 6.4. The time is normalized by 122.2 yr, and the flux Φ is normalized by the magnetic field of 300 G.

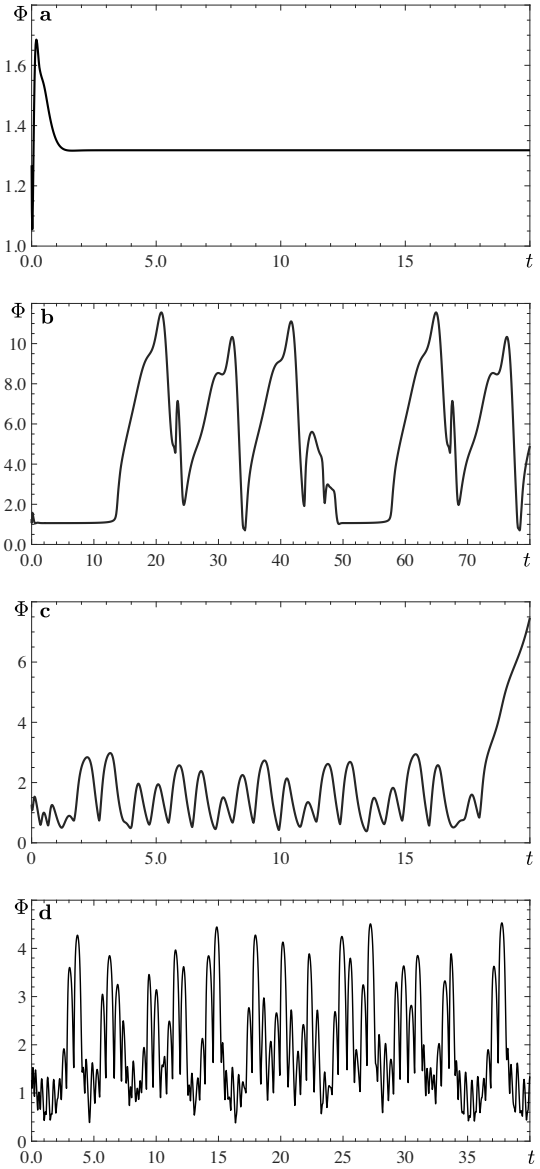

Figure 9. The time evolution of the flux of the toroidal mean magnetic field $\Phi = \int |\overline{B}_\varphi| \, d\sigma$ obtained from numerical simulations of $\alpha^2\Omega$ mean-field dynamo at different values of $R_\omega/R_\alpha = 1.6$ (**a**), 3.2 (**b**), 4.7 (**c**), and 6.4 (**d**). The time is normalized by 122.2 yr, and the flux Φ is normalized by the magnetic field of 300 G.

Note that 122.2 yr corresponds to the turbulent diffusion time R_*^2/η_T with $R_* = R_\odot$ and $\eta_T = 1.4 \times 10^{12}$ cm^2 s^{-1}. Here, we take into account that the integral scale ℓ_0 of the turbulent convection is smaller by a factor 5–7 than the size of the coherent structures (the large-scale circulations). The latter is justified by the results of analytical study (Elperin et al. 2002, 2006a, b) and laboratory experiments (Bukai et al. 2009). This causes the mixing length used in the mixing length theory is about 5–7 times larger than the integral scale ℓ_0 of the turbulent convection. Correspondingly, the turbulent diffusion coefficients should be 5–7 times smaller than those from the mixing length theory.

Increase of R_ω/R_α causes decrease in the periods T_* of the stellar magnetic cycles. This is seen in Fig. 10, where we show the periods T_* of the stellar magnetic cycles normalized by 122.2 yr versus R_ω/R_α, which decreases from about 10^3 to 10 yr depending on the value

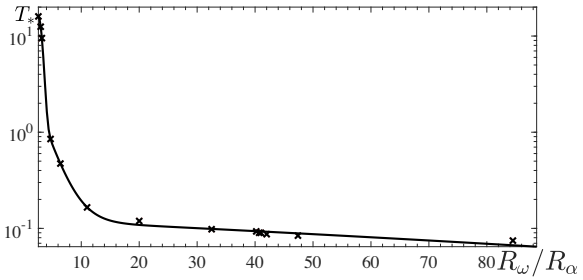

Figure 10. The period T_* of the stellar magnetic cycles normalized by 122.2 yr versus R_ω/R_α obtained from numerical simulations of the non-linear $\alpha^2\Omega$ mean-field dynamo at $R_\alpha = 10$.

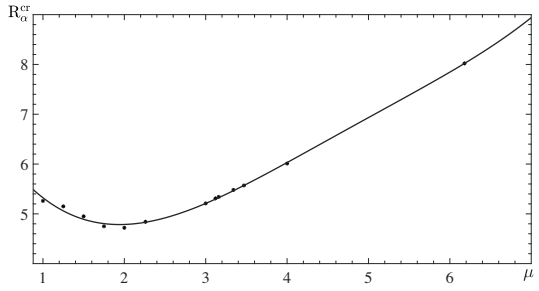

Figure 11. The threshold, R_α^{cr}, in generation of the large-scale magnetic field (snowflakes) versus parameter μ obtained from numerical simulations of the non-linear α^2 mean-field dynamo. Here, the solid line corresponds to the fitting curve.

of the differential rotation. In chaotic regime there can be transition from one attractor with a short period (of several tens years) to that of a larger period (of thousand years), see Fig. 9c. For larger values of R_ω/R_α, the dynamo is similar to the $\alpha\Omega$ mean-field dynamo, while for small values of R_ω/R_α, the dynamo is similar to the α^2 mean-field dynamo.

We will show in the next section that for low-mass main sequences stars rotating much faster than the Sun, the generated large-scale magnetic field is caused by the mean-field $\alpha^2\Omega$ dynamo, whereby the α^2 dynamo is slightly modified by a weak differential rotation. This means that $R_\omega \ll R_\alpha R_\alpha^{cr}$.

3.4 Mean-field numerical simulations of the α^2 dynamo

We also perform numerical simulations of the α^2 mean-field dynamo with $R_\omega = 0$. First, we plot the threshold, R_α^{cr}, required for the generation of the large-scale magnetic field versus

(i) parameter μ (Fig. 11),
(ii) the spectral class (Fig. 12), and
(iii) the stellar effective temperature T_{eff} (Fig. 13),

obtained from numerical simulations. For $\mu \geq 3$, the function $R_\alpha^{cr}(\mu)$ is closed to the linear one (see Fig. 11). Indeed, our asymptotic analysis for a constant kinetic α-effect shows that $R_\alpha^{cr} = (k^2 + \mu^2)^{1/2}$. This implies that when $k^2 \ll \mu^2$, we obtain that $R_\alpha^{cr} \sim \mu$.

In Fig. 12, in addition to the threshold R_α^{cr} versus the stellar spectral class, we also plot the parameter $R_\alpha \equiv \alpha_* R_*/\eta_T = (\Omega_\odot/\eta_T)^{1/2} R_*$ based on the solar rotation rate (see equation 5). As follows from Fig. 12, the parameter R_α is in several times less than the threshold R_α^{cr} required for the generation of the large-scale magnetic field. This implies that the pure α^2 dynamo with the kinetic α-effect $\alpha = (\Omega_\odot \eta_T)^{1/2}$ based on the solar rotation rate cannot explain the

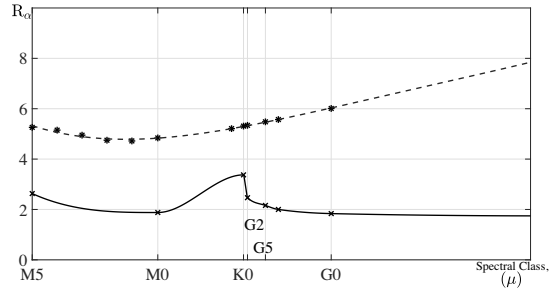

Figure 12. The threshold $R_\alpha^{\rm cr}$ (snowflakes, dashed line) in generation of the large-scale magnetic field and the parameter R_α (crosses, solid line) versus the parameter μ obtained from numerical simulations of the non-linear α^2 mean-field dynamo. The parameter $R_\alpha = (\Omega_\odot/\eta_{\rm T})^{1/2}\, R_*$ is determined for the main sequence stars, where the angular velocity coincides with the mean (averaged over the latitude) solar angular velocity $\Omega_\odot$.

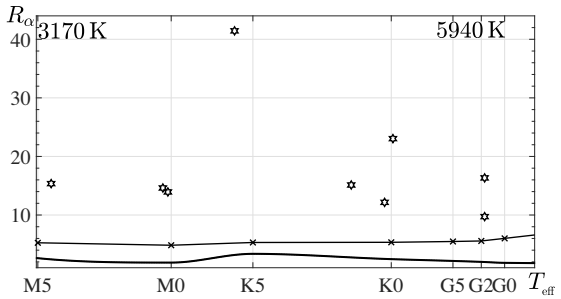

Figure 13. The threshold $R_\alpha^{\rm cr}$ (crosses, thin solid line) in generation of the large-scale magnetic field and the parameter $R_\alpha = \left(\Omega_\odot/\eta_{\rm T}\right)^{1/2}\, R_*$ (solid line) versus the star effective temperature $T_{\rm eff}$ obtained from numerical simulations of the non-linear α^2 mean-field dynamo. The parameter R_α is calculated for the main sequence stars, where the angular velocity coincides with the mean (averaged over the latitude) solar angular velocity $\Omega_\odot$. The parameter $\tilde{R}_\alpha$ (stars) is also estimated for real main sequence stars, where we use equation (5), the rotating rates (see Gershberg et al. 2020) and turbulent magnetic diffusion coefficients for the stars of these spectral classes.

generation of large-scale magnetic field in the main sequences stars. To describe correctly the magnetic field generation in the main sequences stars in the framework of the α^2 dynamo, one need to increase the stellar rotation rate by one order of magnitude to obtain the required value of the α-effect. That is why we consider stars rotating much faster than the Sun.

In Fig. 13, we show the threshold $R_\alpha^{\rm cr}$ (crosses, thin solid line) in generation of the large-scale magnetic field and the parameter $R_\alpha = \left(\Omega_\odot/\eta_{\rm T}\right)^{1/2}\, R_*$ (thick solid line) versus the star effective temperature $T_{\rm eff}$ obtained from numerical simulations of the non-linear α^2 mean-field dynamo. This parameter R_α is calculated for the main sequence stars, where the angular velocity coincides with the mean (averaged over the latitude) solar angular velocity $\Omega_\odot$. In addition, we also show the parameter $\tilde{R}_\alpha$ (shown as stars) that is estimated for real main sequence stars, where we use equation (5), the rotating rates (see Gershberg et al. 2020) and turbulent magnetic diffusion coefficients for the stars of these spectral classes. Fig. 13 demonstrates that the parameter $\tilde{R}_\alpha$ for the observed stars is in several times larger than the threshold $R_\alpha^{\rm cr}$ required for the generation of the large-scale magnetic field by pure α^2 dynamo. This shows that the pure α^2 dynamo can describe the generation of large-scale magnetic field for these stars. However, some observed features (appearance of star spots in the polar regions, long period of cyclic behaviour, etc.) for the main

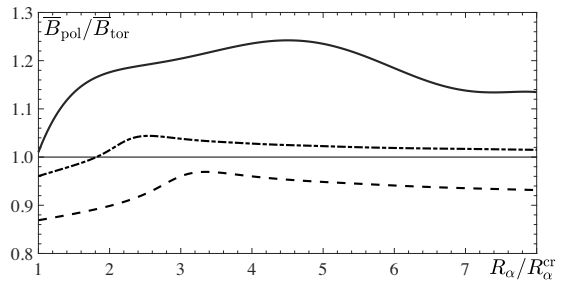

Figure 14. The ratio of the maximum values of the poloidal to toroidal mean magnetic fields $\overline{B}_{\rm pol}/\overline{B}_{\rm tor}$ versus $R_\alpha/R_\alpha^{\rm cr}$ for the main sequence stars of three spectral classes: M5 (solid); M0 (dashed–dotted); K5 (dashed), obtained from numerical simulations of the non-linear α^2 mean-field dynamo.

sequence fast rotating stars require presence of small differential rotation.

In Fig. 14, we show the ratio of the maximum values of the poloidal to toroidal mean magnetic field $\overline{B}_{\rm pol}/\overline{B}_{\rm tor}$ versus $R_\alpha/R_\alpha^{\rm cr}$ for the main sequence stars of three spectral classes: M5, M0, and K5, obtained from numerical simulations in non-linear saturated stage. It seen that in non-linear saturated stage $\overline{B}_{\rm pol}/\overline{B}_{\rm tor} \sim 1$. This is in agreement with equation (14) for $R_\omega \ll R_\alpha R_\alpha^{\rm cr}$ derived for the mean-field $\alpha^2\Omega$ dynamo. The latter implies that the generated large-scale magnetic field is caused by the mean-field $\alpha^2\Omega$ dynamo, whereby the α^2 dynamo is modified by a weak differential rotation.

4 NON-LINEAR THEORY OF AXISYMMETRIC α^2 DYNAMO

In this section, we discuss a non-linear theory of axisymmetric α^2 dynamo. We consider the axisymmetric mean-field α^2 dynamo in spherical coordinates. The non-linear mean-field induction equation reads

$$\frac{\partial}{\partial t}\begin{pmatrix} A \\ B \end{pmatrix} = \left(\hat{L} + \hat{N}\right)\begin{pmatrix} A \\ B \end{pmatrix}, \tag{27}$$

where

$$\hat{L} = \begin{pmatrix} \Delta_{\rm s} & \alpha_{\rm k}(r,\theta) \\ -R_\alpha^2\Delta_{\alpha_{\rm k}} & \Delta_{\rm s} \end{pmatrix}, \tag{28}$$

$$\hat{N} = \begin{pmatrix} 0 & \alpha_{\rm m}(r,\theta) \\ -R_\alpha^2\Delta_{\alpha_{\rm m}} & 0 \end{pmatrix}, \tag{29}$$

and

$$\Delta_{\rm s}\tilde{\Phi} = \frac{1}{r}\frac{\partial^2}{\partial r^2}(r\tilde{\Phi}) + \frac{1}{r^2}\frac{\partial}{\partial\theta}\left(\frac{1}{\sin\theta}\frac{\partial}{\partial\theta}(\sin\theta\,\tilde{\Phi})\right) \equiv \left(\Delta - \frac{1}{r^2\sin^2\theta}\right)\tilde{\Phi},$$

and

$$\Delta_{\alpha_{\rm k,m}}\tilde{\Phi} = \frac{1}{r}\frac{\partial}{\partial r}\left(\alpha_{\rm k,m}\frac{\partial}{\partial r}(r\tilde{\Phi})\right) + \frac{1}{r^2}\frac{\partial}{\partial\theta}\left(\frac{\alpha_{\rm k,m}}{\sin\theta}\frac{\partial}{\partial\theta}(\sin\theta\,\tilde{\Phi})\right).$$

Equations (27)–(29) are written in dimensionless variables (see Section 3). The operator $\hat{L}$ describes the kinematic dynamo. Here, $\alpha_{\rm k}(r,\theta) = -\alpha_{\rm k}(r,\pi-\theta)$.

We neglect algebraic quenching of the kinetic and magnetic α-effect, but take into account the dynamical non-linearity related to the conservation law of the total magnetic helicity for very large

magnetic Reynolds numbers. The magnetic α-effect is determined by the evolutionary equation

$$\frac{\partial \alpha_{\rm m}}{\partial t} + \frac{\alpha_{\rm m}}{T_\alpha} = \nabla \cdot \left(\kappa_T \nabla \alpha_{\rm m}\right) - \frac{2}{\rho}\left[(\alpha_{\rm k} + \alpha_{\rm m})\, R_\alpha^2\, \overline{\boldsymbol{B}}_p^2 - \hat{M}(B, A) + B\,\frac{\partial A}{\partial t}\right], \tag{30}$$

where $\overline{\boldsymbol{B}}_p = {\rm rot}[A(t, r, \theta)\boldsymbol{e}_\varphi]$ is the poloidal component of the mean magnetic field, and

$$\hat{M}(B, A) = {\rm rot}\left(B\,\boldsymbol{e}_\varphi\right) \cdot {\rm rot}\left(A\,\boldsymbol{e}_\varphi\right).$$

We seek a solution of the non-linear equations (27) and (30) in the following form:

$$\begin{pmatrix} A \\ B \end{pmatrix} = \sum_{n=1}^{\infty} F^n(t)\mathbf{e}_n(r, \theta), \quad \mathbf{e}_n = \begin{pmatrix} a_n \\ b_n \end{pmatrix}, \tag{31}$$

where $\boldsymbol{e}_n$ are the eigenvectors of the operator $\hat{L}$ for $R_\alpha = R_\alpha^{\rm cr}$, i.e. $\hat{L}^{\rm cr}\boldsymbol{e}_n = p_n^{\rm cr}\boldsymbol{e}_n$. Substituting equation (31) into equation (27) and taking into account the properties of the eigenvectors , we obtain the following system of equations for the coefficients $F^\ell(t)$ in equation (31):

$$\frac{{\rm d}F^\ell}{{\rm d}t} - F^\ell\, p_\ell^{\rm cr} = \frac{1}{2}\left(\frac{{\rm d}p_\ell}{{\rm d}\ln R_\alpha}\right)_{\rm cr} \sum_{n=-\infty}^{\infty} F^n(t)\Big[\alpha_n^\ell + R_\alpha^2\,\tilde{\alpha}_n^\ell + \left[R_\alpha^2 - (R_\alpha^{\rm cr})^2\right]\, G_n^\ell\Big], \tag{32}$$

where $p_\ell^{\rm cr} = p_\ell\left(R_\alpha = R_\alpha^{\rm cr}\right)$, and functions $\alpha_n^\ell, \tilde{\alpha}_n^\ell$, and G_n^ℓ are defined by equations (B1)–(B3) in Appendix B.

The coefficients $F^\ell(t)$ depend on the non-linearity characterized by α_n^ℓ. The equation for α_n^ℓ is derived from equation (30):

$$\frac{{\rm d}\alpha_n^\ell}{{\rm d}t} + \frac{\alpha_n^\ell}{T_\alpha} = -2\sum_{k,s=-\infty}^{\infty} F^k(t)\left\{\frac{{\rm d}F^s}{{\rm d}t} S_{\rm ksn}^\ell - F^s\left[M_{\rm ksn}^\ell - R_\alpha^2\left(\frac{\alpha_n^\ell}{t_\chi} + K_n^\ell\right)(\overline{\boldsymbol{b}}_p)_k(\overline{\boldsymbol{b}}_p)_s\right]\right\} - 2\kappa_T\left(C_1\alpha_n^\ell - \tilde{\alpha}_n^\ell\right), \tag{33}$$

where $(\overline{\boldsymbol{b}}_p)_n = {\rm rot}\left(a_n\,\boldsymbol{e}_\varphi\right)$, and the tensors $M_{\rm ksn}^\ell$, $S_{\rm ksn}^\ell$, and K_n^ℓ are determined by equations (B5)–(B8) in Appendix A. The equation for $\tilde{\alpha}_n^\ell$ is derived from equation (30) as well:

$$\frac{{\rm d}\tilde{\alpha}_n^\ell}{{\rm d}t} + \frac{\tilde{\alpha}_n^\ell}{T_\alpha} = -2\sum_{k,s=-\infty}^{\infty} F^k(t)\left\{\frac{{\rm d}F^s}{{\rm d}t}\tilde{S}_{\rm ksn}^\ell - F^s\left[\tilde{M}_{\rm ksn}^\ell - R_\alpha^2\left(\frac{\tilde{\alpha}_n^\ell}{\tilde{t}_\chi} + \tilde{K}_n^\ell\right)(\overline{\boldsymbol{b}}_p)_k(\overline{\boldsymbol{b}}_p)_s\right]\right\} - \kappa_{\rm T} C_2\tilde{\alpha}_n^\ell, \tag{34}$$

where the functions $\tilde{M}_{\rm ksn}^\ell$, $\tilde{S}_{\rm ksn}^\ell$, $\tilde{K}_n^\ell$ are determined by equations (B9)–(B11) in Appendix B. It is assumed here that the relaxation time T_α of the magnetic helicity is independent of $\mathbf{r}$. Thus, the problem reduces to the study of this infinite system of equations with coefficients determined by the eigenfunctions and eigenvalues of the linear problem for $R_\alpha = R_\alpha^{\rm cr}$. When R_α in the stellar convective zone is not much larger than the critical value $R_\alpha^{\rm cr}$ required for the excitation of the dynamo instability, only few modes are excited.

Let us consider the simplest case, when only one mode is excited. This is sufficient to estimate the magnitude of the mean magnetic field in a steady state. The multi-mode regime could be considered similarly. The equations of the single-mode approximation follow from equations (32)–(34):

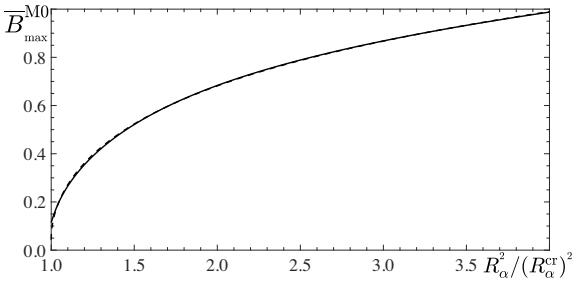

Figure 15. The maximum mean magnetic field $\overline{B}_{\rm max}^{\rm M0}$ versus $(R_\alpha/R_\alpha^{\rm cr})^2$ for the main sequence stars of the spectral class M0, obtained from numerical simulations (solid) of the non-linear α^2 mean-field dynamo and analytical result (dashed) described by equations (38) and (39).

$$\frac{{\rm d}F}{{\rm d}t} - F p^{\rm cr} = F(t)\Big[\left[R_\alpha^2 - (R_\alpha^{\rm cr})^2\right]\, G + \alpha + R_\alpha^2\,\tilde{\alpha}\Big], \tag{35}$$

$$\frac{{\rm d}\alpha}{{\rm d}t} + \frac{\alpha}{T_\alpha} + \kappa_T\left(C_1\alpha - \tilde{\alpha}\right) = -\frac{1}{2}\frac{{\rm d}F^2}{{\rm d}t} S + F^2\left[M - R_\alpha^2\left(K + \frac{\alpha}{t_\chi}\overline{\boldsymbol{b}}_p^2\right)\right], \tag{36}$$

$$\frac{{\rm d}\tilde{\alpha}}{{\rm d}t} + \frac{\tilde{\alpha}}{T_\alpha} + \kappa_{\rm T} C_2\tilde{\alpha} = F^2\left[\tilde{M} - R_\alpha^2\left(\tilde{K} + \frac{\tilde{\alpha}}{\tilde{t}_\chi}\overline{\boldsymbol{b}}_p^2\right)\right] - \frac{1}{2}\frac{{\rm d}F^2}{{\rm d}t}\tilde{S}, \tag{37}$$

The steady-state solution of equations (35)–(37) for this single-mode approximation yields the magnitude of the mean toroidal magnetic field near the stellar surface as

$$\overline{B} = \left(2\pi\overline{\rho}_*\right)^{1/2}\frac{3\eta_{\rm T}\,\kappa_{\rm T}}{R_*}\left(\frac{2G\,T_\alpha}{K}\right)^{1/2} f\left[\frac{R_\alpha^2}{(R_\alpha^{\rm cr})^2}\right], \tag{38}$$

where

$$f(X) = \left(\frac{X-1}{X-C}\right)^{1/2}\left[(R_\alpha^{\rm cr})^2 X + 2\right]^{-1} \times\left[1 - 2G\,\frac{(R_\alpha^{\rm cr})^2 X(X-1)}{(X-C)\left[(R_\alpha^{\rm cr})^2 X + 2\right]}\,\frac{\overline{\boldsymbol{b}}_p^2}{t_\chi} + \left(1 - 4G\,\frac{(R_\alpha^{\rm cr})^2 X(X-1)}{(X-C)\left[(R_\alpha^{\rm cr})^2 X + 2\right]}\,\frac{\overline{\boldsymbol{b}}_p^2}{t_\chi}\right)^{1/2}\right]^{-1/2}, \tag{39}$$

and we consider the case when $K \approx \tilde{K}$, $M \approx \tilde{M}$, $K/M = C$, $t_\chi \approx \tilde{t}_\chi$, and $C_1 = C_2 = 1$. The characteristic times t_χ and $\tilde{t}_\chi$ are defined by equations (B8) and (B12) in Appendix B.

In Fig. 15, we show the maximum mean magnetic field $\overline{B}_{\rm max}^{\rm M0}$ (solid) versus $(R_\alpha^2/R_\alpha^{\rm cr})^2$ for the main sequence stars of the spectral class M0 obtained from the MFS, that is in an agreement with analytical result (dashed) described by equations (38) and (39).

5 DISCUSSIONS AND CONCLUSIONS

We start the discussion with some comments related to various numerical simulations. There are two different kinds of numerical simulations discussed in this paper which are very important for investigations of the stellar magnetic activity. The first kind of simulations is DNS and LES (see, e.g. Dobler et al. 2006; Browning 2008; Yadav et al. 2016; Brown et al. 2020; Käpylä 2021; Bice & Toomre 2022; Käpylä et al. 2023). The DNS and LES solve exact (or nearly exact) equations and demonstrate physical effects which

mimic the processes occurring inside stars. For instance, the key feature of the DNS and LES which investigate the stellar magnetic activity, is that they study small-scale turbulent effects and their influence to large-scale magnetic activity. However, the used range for the key parameters (e.g. fluid and magnetic Reynolds numbers, Péclet number, Rayleigh number, degree of density stratification, etc.) which can be achieved in the DNS and LES, is essentially different from the parameter range which is typical for stars (see, e.g. review by Käpylä et al. 2023).

The second type of simulations is MFS (see, e.g. Chabrier & Küker 2006; Kitchatinov et al. 2014; Shulyak et al. 2015; Pipin 2017; Pipin & Yokoi 2018), which are based on various mean-field theories and take into account various turbulence effects by means of turbulent transport coefficients (e.g. turbulent viscosity, turbulent magnetic diffusivity, turbulent heat conductivity, the alpha effect, the lambda effect, etc). The MFS allow to study the large-scale and long-term effects in spatial and time scales which are much larger than the turbulent scales. Mean-field models have been tested using various solar and geophysical observations of magnetic activity. Note also that mean-field models are usually improved using the results of the DNS and LES.

In this paper in addition to the analytical study, we perform non-linear MFS. Thus, we can compare our model with others MFS. In particular, some studies (Chabrier & Küker 2006; Kitchatinov et al. 2014; Shulyak et al. 2015) mainly investigate the kinematic (linear) stage of the mean-field dynamo instabilities, while in our paper we study non-linear mean-field dynamo instabilities, taking into account algebraic and dynamic non-linearities.

Pipin (2017) has performed the MFS of the non-linear axisymmetric and non-axisymmetric $\alpha^2\Omega$ dynamos of the fully convective star. However, the dynamical quenching of the α-effect is determined in this dynamo model by equation for the total magnetic helicity density rather than that for the evolution of magnetic helicity density of the small-scale field. The latter is a weak point of this non-linear dynamo model, because the magnetic α-effect is determined by the evolution of the current helicity of the small-scale field, which is caused by the production and transport of the magnetic helicity density of the small-scale magnetic field.

In this study, we investigate the non-linear axisymmetric $\alpha^2\Omega$ and α^2 dynamos using the dynamic equation for the evolution of magnetic helicity density of the small-scale field. We compare the results of the performed MFS with the developed non-linear theory of mean-field dynamo. In particular, the derived scaling for the magnitude of the mean toroidal magnetic field near the stellar surface as a function of various key parameters is in agreement with the results of the performed MFS (see, e.g. Fig. 15).

A majority of the observed stars are fast rotating, because much more easy to observe fast rotating stars generated strong magnetic fields. Our theoretical study and mean-field numerical simulations suggest that for fast rotating low-mass main sequences stars with the spectral classes from M5 to G5, the generated large-scale magnetic field is caused by the mean-field $\alpha^2\Omega$ dynamo, where the α^2 dynamo is modified by a weak differential rotation. The latter implies that $R_\omega \ll R_\alpha R_\alpha^{\rm cr}$. However, even a weak differential rotation in the non-linear phase of magnetic field evolution causes drastic changes in magnetic activity, resulting in chaotic behaviour where long-term evolution (with the period about thousand years) is accompanied by fast changes of the several tens years.

In view of observations, this multi-time-scale system causes very complicated patters in magnetic activity, e.g. the fast rotating stars with the same rotation rates and the same spectral classes may have different magnetic activity. This implies necessity of long-term observational programs of the stellar magnetic activity. The long-term behaviour of the magnetic activity is related to the characteristic time of the evolution of the magnetic helicity density of the small-scale magnetic field. The performed MFS have shown that the kinematic and non-linear phases of magnetic field evolution are very different. For instance, non-linear effects cause a threshold in the differential rotation that is necessary for a transition between aperiodic and quasi-periodic regime. We demonstrate that period of non-linear oscillations decreases with increase of the differential rotation.

ACKNOWLEDGEMENTS

The work of NK and NS was supported by the Russian Science Foundation (grant 21-72-20067). IR acknowledges the hospitality of NORDITA.

DATA AVAILABILITY

The data that support the findings of this study are available from the corresponding author upon reasonable request.

REFERENCES

Baker N., Temesvary S., 1966, Tables of Convective Stellar Envelope Models, 2nd edn., Goddard Institute for Space Studies, New York
Bassom A. P., Kuzanyan K. M., Sokoloff D., Soward A. M., 2005, GAFD, 99, 309
Bice C. P., Toomre J., 2022, ApJ, 928, 51
Blackman E. G., Field G. B., 2000, ApJ, 534, 984
Bochanski J. J., Hawley S. L., Covey K. R., West A. A., Reid I. N., Golimowski D. A., Ivezic Z., 2010, AJ, 139, 2679
Bondar' N. I., Katsova M. M., Livshits M. A., 2019, Geomagn. Aeron., 59, 832
Brandenburg A., Gressel O., Käpylä P. J., Kleeorin N., Mantere M. J., Rogachevskii I., 2013, ApJ, 762, 127
Brandenburg A., Kemel K., Kleeorin N., Mitra D., Rogachevskii I., 2011, ApJ, 740, L50
Brandenburg A., Rogachevskii I., Kleeorin N., 2016, New J. Phys., 1812, 5011
Brandenburg A., Subramanian K., 2005, Phys. Rep., 417, 1
Brown B. P., Oishi J. S., Vasil G. M. Lacoanet D. Burns K. J. 2020, ApJ, 902, L3
Browning M. K., 2008, ApJ, 676, 1262
Bukai M., Eidelman A., Elperin T., Kleeorin N., Rogachevskii I., Sapir-Katiraie I., 2009, Phys. Rev. E, 79, 066302
Chabrier G., Küker M., 2006, A&A, 446, 1027
Cox J. P., Giuli R. T., 1968, Principles of Stellar Structure, Gordon & Breach, New York
Dobler W., Stix M., Brandenburg A., 2006, ApJ, 638, 336
Donati J.-F. et al., 2003, MNRAS, 345, 1145
Donati J.-F., Morin J., Petit P., Delfosse X., 2008, MNRAS, 390, 545
Elperin T., Golubev I., Kleeorin N., Rogachevskii I., 2006b, Phys. Fluids, 18, 126601
Elperin T., Kleeorin N., Rogachevskii I., Zilitinkevich S., 2002, Phys. Rev. E, 66, 066305
Elperin T., Kleeorin N., Rogachevskii I., Zilitinkevich S., 2006a, Bound.-Layer Meteorol., 119, 449
Field G. B., Blackman E. G., Chou H., 1999, ApJ, 513, 638
Frisch U., Pouquet A., Leorat I., Mazure A., 1975, J. Fluid Mech., 68, 769
Gastine T., Duarte L., Wicht J., 2012, A&A, 546, A19
Gershberg R. E., Kleeorin N., Pustilnik L. A., Shlapnikov A. A., 2020, Physics of Middle- and Low-Mass Stars with Solar Activity Type, Nauka, Moscow
Gopalakrishnan K., Subramanian K., 2023, ApJ, 8, 65

Griffiths G. L., Bassom A. P., Soward A. M., Kuzanyan K. M., 2001, GAFD, 94, 85
Gruzinov A. V., Diamond P. H., 1994, Phys. Rev. Lett., 72, 1651
Hawley S. L., Davenport J. R. A., Kowalski A. F., Wisniewski J. P., Hebb L., Deitrick R., Hilton E. J., 2014, ApJ, 797, 121
Henyey L. G., Vardya M. S., Bodenheimer P., 1965, ApJ, 142, 841
Käpylä P. J., 2021, A &A, 65, A66
Käpylä P. J., Browning M. K., Brun A. S., Guerrero G., Warnecke J., 2023, preprint (arXiv:2305.16790)
Kitchatinov L. L., Moss D., Sokoloff D., 2014, MNRAS, 442, L1
Kitchatinov L. L., Olemskoy S. V., 2011, MNRAS, 411, 1059
Kleeorin N., Kuzanyan K., Moss D., Rogachevskii I., Sokoloff D., Zhang H., 2003a, A&A, 409, 1097
Kleeorin N., Mond M., Rogachevskii I., 1996, A&A, 307, 293
Kleeorin N., Moss D., Rogachevskii I., Sokoloff D., 2000, A&A, 361, L5
Kleeorin N., Moss D., Rogachevskii I., Sokoloff D., 2002, A&A, 387, 453
Kleeorin N., Moss D., Rogachevskii I., Sokoloff D., 2003b, A&A, 400, 9
Kleeorin N., Rogachevskii I., 1994, Phys. Rev. E, 50, 2716
Kleeorin N., Rogachevskii I., 1999, Phys. Rev. E, 59, 6724
Kleeorin N., Rogachevskii I., 2003, Phys. Rev. E, 67, 026321
Kleeorin N., Rogachevskii I., 2022, MNRAS, 515, 5437
Kleeorin N., Rogachevskii I., Ruzmaikin A. A., 1989, Sov. Astron. Lett., 15, 274
Kleeorin N., Rogachevskii I., Ruzmaikin A. A., 1990, J. Exp. Theor. Phys., 70, 878
Kleeorin N., Rogachevskii I., Ruzmaikin A., 1995, A&A, 297, 159
Kleeorin N., Ruzmaikin A., 1982, Magnetohydrodynamics, 18, 116
Kleeorin N., Safiullin N., Kuzanyan K. M., Rogachevskii I., Tlatov A., Porshnev S., 2020, MNRAS, 495, 238
Kleeorin Y., Safiullin N., Kleeorin N., Porshnev S., Rogachevskii I., Sokoloff D., 2016, MNRAS, 460, 3960
Kochukhov O., 2021, A&AR, 29, 1
Kochukhov O., Hachman T., Lehtinen J. J., Wehrhahn A., 2020, A&A, 635, A142
Krause F., Rädler K.-H., 1980, Mean-Field Magnetohydrodynamics and Dynamo Theory, Pergamon, Oxford
Meunier N., , Nesme-Ribes E., Sokoloff D. 1996, Astron. Rep., 40, 415
Moffatt H. K., 1978, Magnetic Field Generation in Electrically Conducting Fluids, Cambridge Univ. Press, Cambridge
Moffatt H. K., Dormy E., 2019, Self-Exciting Fluid Dynamos, Cambridge Univ. Press, Cambridge
Morin J., Donati J.-F., Petit P., Delfosse X. Forveille T. Jardine M. M. 2010, MNRAS, 407, 2269
Newton E. R., Irwin J., Charbonneau D., Berlind P., Calkins M. L., Mink J., 2017, ApJ, 834, 85
Parker E., 1979, Cosmical Magnetic Fields, Clarendon, Oxford
Paxton B., Bildsten L., Dotter A., Herwig F., Lesaffre P., Timmes F., 2011, ApJS, 192, 3
Pecaut M. J., Mamajek E. E., 2013, ApJS, 208, 9
Pipin V. V., 2017, MNRAS, 466, 3007
Pipin V. V., Yokoi N., 2018, ApJ, 859, 18
Pouquet A., Frisch U., Leorat J., 1976, J. Fluid Mech., 77, 321
Reiners A., Basri G., 2007, ApJ, 656, 1121
Rogachevskii I., 2021, Introduction to Turbulent Transport of Particles, Temperature and Magnetic Fields, Cambridge Univ. Press, Cambridge
Rogachevskii I., Kleeorin N., 2000, Phys. Rev. E, 61, 5202
Rogachevskii I., Kleeorin N., 2001, Phys. Rev. E., 64, 056307
Rogachevskii I., Kleeorin N., 2004, Phys. Rev. E, 70, 046310
Rogachevskii I., Kleeorin N., 2006, Geophys. Astrophys. Fluid Dyn., 100, 243
Rogachevskii I., Kleeorin N., 2007, Phys. Rev. E, 76, 056307
Rüdiger G., Hollerbach R., Kitchatinov L. L., 2013, Magnetic Processes in Astrophysics: Theory, Simulations, Experiments, John Wiley & Sons, Weinheim
Ruzmaikin A., Shukurov A. M., Sokoloff D. D., 1988, Magnetic Fields of Galaxies, Kluwer Academic, Dordrecht
Saar S. H., 1996, in Uchida Y., Kosugi T., Hudson H. S., eds, Proc. IAU Symp. 153, Magnetodynamic Phenomena in the Solar Atmosphere. Kluwer, Dordrecht
Saar S. H., Linsky J. L., 1985, ApJ, 299, L47
Safiullin N., Kleeorin N., Porshnev S., Rogachevskii I., Ruzmaikin A., 2018, J. Plasma Phys., 84, 735840306
Schrinner M., Petitdemange L., Dormy E., 2012, ApJ, 752, 121
Shukurov A., Subramanian K., 2021, Astrophysical Magnetic Fields: From Galaxies to the Early Universe. Cambridge Univ. Press, Cambridge
Shulyak D., Sokoloff D., Kitchatinov L., Moss D., 2015, MNRAS, 449, 3471
Spruit H. C., 1974, Sol. Phys., 34, 277
Strassmeier K. G., 2009, A&AR, 17, 251
Warnecke J., Losada I. R., Brandenburg A., Kleeorin N., Rogachevskii I., 2013, ApJ, 777, L37
Warnecke J., Losada I. R., Brandenburg A., Kleeorin N., Rogachevskii I., 2016, A&A, 589, A125
Winters J. G. et al., 2019, AJ, 157, 216
Wright N. J., Newton E. R., Williams P. K. G., Drake J. J., Yadav R. K., 2018, MNRAS, 479, 2351
Yadav R. K., Christensen U. R., Morin J., Gastine T., Reiners A., Poppenhaeger K., Wolk S. J., 2015, ApJ, 813, L31
Yadav R. K., Christensen U. R., Wolk S. J., Poppenhaeger K., 2016, ApJ, 833, L28
Zeldovich Ya. B., Ruzmaikin A. A., Sokoloff D. D., 1983, Magnetic Fields in Astrophysics. Gordon and Breach, New York
Zhang H., Moss D., Kleeorin N., Kuzanyan K., Rogachevskii I., Sokoloff D., Gao Y., Xu H., 2012, ApJ, 751, 47
Zhang H., Sokoloff D., Rogachevskii I., Moss D., Lamburt V., Kuzanyan K., Kleeorin N., 2006, MNRAS, 365, 276

APPENDIX A: THE FUNCTIONS $\Psi_1(\omega)$ AND $\Psi_2(\omega)$

The functions $\Psi_1(\omega)$ and $\Psi_2(\omega)$ are given by

$$\Psi_1(\omega) = (3-\sigma)\left[4A_1^{(3)}(2\omega) - \frac{3}{\pi}\bar{A}_1(\omega^2)\right] - \frac{\lambda}{2}\left[4A_1^{(2)}(2\omega) - A_1^{(2)}(\omega)\right] + 3(\sigma-1)\left[4C_1^{(3)}(2\omega) - \frac{3}{\pi}\bar{C}_1(\omega^2)\right],$$

$$\Psi_2(\omega) = 3(\sigma-1)\left[4C_3^{(3)}(2\omega) - \frac{3}{\pi}\bar{C}_3(\omega^2)\right].$$

where

$$A_1^{(2)}(\omega) = 6\left[\frac{\arctan(\omega)}{\omega}\left(1+\frac{1}{\omega^2}\right) - \frac{3}{\omega^2} + \frac{2}{\omega^3}S(\omega)\right],$$

$$A_1^{(3)}(\omega) = J_0^{(3)}(\omega) - J_2^{(3)}(\omega),$$

$$C_1^{(3)}(\omega) = \frac{1}{4}\left[J_0^{(3)}(\omega) - 2J_2^{(3)}(\omega) + J_4^{(3)}(\omega)\right],$$

$$C_3^{(3)}(\omega) = \frac{1}{4}\left[-J_0^{(3)}(\omega) + 6J_2^{(3)}(\omega) - 5J_4^{(3)}(\omega)\right],$$

and

$$\bar{A}_1(\omega^2) = \frac{2\pi}{\omega^2}\left[(\omega^2+1)\frac{\arctan(\omega)}{\omega} - 1\right],$$

$$\bar{C}_1(\omega^2) = \frac{\pi}{2\omega^4}\left[(\omega^2+1)^2\frac{\arctan(\omega)}{\omega} - \frac{5\omega^2}{3} - 1\right],$$

$$\bar{C}_3(\omega^2) = -\frac{\pi}{2\omega^4}\left[\left[\omega^4+6\omega^2+5\right]\frac{\arctan(\omega)}{\omega} - \frac{13\omega^2}{3} - 5\right].$$

where

$$J_0^{(3)}(\omega) = 2\left[2\frac{\arctan(\omega)}{\omega} + \frac{1}{\omega^4}\ln\left(1+\omega^2\right) - \frac{1}{\omega^2}\right],$$

$$J_2^{(3)}(\omega) = \frac{6}{\omega^2}\left[1 - 2\frac{\arctan(\omega)}{\omega} + \frac{1}{\omega^2}\ln\left(1+\omega^2\right)\right],$$

$$J_4^{(3)}(\omega) = \frac{2}{\omega^2}\left[1 - \frac{3}{\omega^2}\left(2\frac{\arctan(\omega)}{\omega} - 2 + \ln\left(1+\omega^2\right)\right)\right],$$

and $S(\omega) = \int_0^\omega [\arctan(y)/y]\,\mathrm{d}y$.

In the case of $\omega \ll 1$ these functions are given by

$$A_1^{(2)}(\omega) = \frac{8}{3}\left(1 - \frac{3\omega^2}{25}\right),$$
$$A_1^{(3)}(\omega) = 2\left(1 - \frac{2\omega^2}{15}\right),$$
$$C_1^{(3)}(\omega) = \frac{2}{5}\left(1 - \frac{2\omega^2}{21}\right), \quad C_3^{(3)}(\omega) = -\frac{8}{105}\,\omega^2,$$
$$J_0^{(3)}(\omega) = 3\left(1 - \frac{2\omega^2}{9} + \frac{\omega^4}{10}\right),$$
$$J_2^{(3)}(\omega) = 1 - \frac{2\omega^2}{5} + \frac{3\omega^4}{14},$$
$$J_4^{(3)}(\omega) = \frac{3}{5}\left(1 - \frac{10\omega^2}{21} + \frac{5\omega^4}{18}\right),$$

In the case of $\omega \gg 1$ these functions are given by

$$A_1^{(2)}(\omega) = \frac{3\pi}{\omega} - \frac{24}{\omega^2}, \quad A_1^{(3)}(\omega) = \frac{2\pi}{\omega},$$
$$C_1^{(3)}(\omega) = \frac{\pi}{2\omega}, \quad C_3^{(3)}(\omega) = -\frac{\pi}{2\omega},$$
$$J_0^{(3)}(\omega) = \frac{2\pi}{\omega} - \frac{6}{\omega^2}, \quad J_2^{(3)}(\omega) = \frac{6}{\omega^2}, \quad J_4^{(3)}(\omega) = \frac{2}{\omega^2}.$$

In the case of $\omega^2 \ll 1$ these functions are given by

$$\bar{A}_1(\omega^2) \sim \frac{4\pi}{3}\left(1 - \frac{\omega^2}{5}\right), \quad \bar{A}_2(\omega^2) \sim -\frac{8\pi}{15}\,\omega^2,$$
$$\bar{C}_1(\omega^2) \sim \frac{4\pi}{15}\left(1 - \frac{\omega^2}{7}\right), \quad \bar{C}_2(\omega^2) \sim \frac{32\pi}{315}\,\omega^4,$$
$$\bar{C}_3(\omega^2) \sim -\frac{8\pi}{105}\,\omega^2.$$

In the case of $\omega^2 \gg 1$ these functions are given by

$$\bar{A}_1(\omega^2) \sim \frac{\pi^2}{\omega}, \quad \bar{A}_2(\omega^2) \sim -\frac{\pi^2}{\omega},$$
$$\bar{C}_1(\omega^2) \sim \frac{\pi^2}{4\omega} - \frac{4\pi}{3\omega^2}, \quad \bar{C}_2(\omega^2) \sim \frac{3\pi^2}{4\omega},$$
$$\bar{C}_3(\omega^2) \sim -\frac{\pi^2}{4\omega} + \frac{8\pi}{3\omega^2}.$$

APPENDIX B: FUNCTIONS FOR AXI-SYMMETRIC NON-LINEAR α^2 DYNAMO

The functions α_n^ℓ, $\tilde{\alpha}_n^\ell$ and G_n^ℓ entering in equation (32), are given by

$$\alpha_n^\ell = Q_\ell^{-1} \int \alpha_{\rm m}\, a^{\ell,*}\, b_n\, d^3r, \tag{B1}$$
$$\tilde{\alpha}_n^\ell = Q_\ell^{-1} \int \alpha_{\rm m}\, \hat{M}(b^{\ell,*}, a_n)\, d^3r, \tag{B2}$$
$$G_n^\ell = Q_\ell^{-1} \int \alpha_{\rm k}\, \hat{M}(b^{\ell,*}, a_n)\, d^3r, \tag{B3}$$
$$Q_\ell = \int \alpha_{\rm k}\, a^{\ell,*}\, b_\ell\, d^3r. \tag{B4}$$

The tensors $M_{\rm ksn}^\ell$, $S_{\rm ksn}^\ell$, and K_n^ℓ entering in equation (33) are given by

$$M_{ksn}^\ell = Q_\ell^{-1} \int \frac{\hat{M}(b_k, a_s)}{\rho(r)}\, a^{\ell,*}\, b_n\, d^3r, \tag{B5}$$
$$S_{ksn}^\ell = Q_\ell^{-1} \int \frac{1}{\rho(r)}\, a^{\ell,*}\, b_n b_k a_s\, d^3r, \tag{B6}$$
$$K_n^\ell = Q_\ell^{-1} \int \frac{\alpha_{\rm k}}{\rho(r)}\, a^{\ell,*}\, b_n\, d^3r, \tag{B7}$$
$$t_\chi^{-1} = Q_\ell^{-1} \int a^{\ell,*}\, b_n\, d^3r. \tag{B8}$$

The tensors $\tilde{M}_{\rm ksn}^\ell$, $\tilde{S}_{\rm ksn}^\ell$, $\tilde{K}_n^\ell$ entering in equation (34) are given by

$$\tilde{M}_{ksn}^\ell = Q_\ell^{-1} \int \frac{1}{\rho(r)}\, \hat{M}(b_k, a_s)\, \hat{M}(b^{\ell,*}, a_n)\, d^3r, \tag{B9}$$
$$\tilde{S}_{ksn}^\ell = Q_\ell^{-1} \int \frac{1}{\rho(r)}\, \hat{M}(b^{\ell,*}, a_n)\, b_k\, a_s\, d^3r, \tag{B10}$$
$$\tilde{K}_n^\ell = Q_\ell^{-1} \int \frac{\alpha_{\rm k}}{\rho(r)}\, \hat{M}(b^{\ell,*}, a_n)\, d^3r, \tag{B11}$$
$$\tilde{t}_\chi^{-1} = Q_\ell^{-1} \int \frac{1}{\rho(r)}\, \hat{M}(b^{\ell,*}, a_n)\, d^3r. \tag{B12}$$

This paper has been typeset from a TEX/LATEX file prepared by the author.